Proceedings of the 11th World Congress on New Technologies (NewTech'25)
Paris, France - August, 2025
Paper No. ICBB 160
DOI: 10.11159/icbb25.160

BARG: A Boosted Adaptive Radial Proximity Method for Graph Modelling in Breast Cancer Hormonal Status Classification

Atefeh Azin Kousha[1]
[1] School of Science, Computing and Engineering Technologies, Swinburne University of Technology, Melbourne, VIC 3122, Australia
aazinkousha@swin.edu.au

Abstract **-** Graph Convolutional Networks (GCNs) perform best on homophilic graphs, where connected nodes share similar features; however, histopathology images pose a challenge due to their heterogeneous tissue patterns and diverse morphological structures. In such images, ensuring homophily is crucial because, in non-homophilic graphs, message passing can cause over-smoothing, where features from dissimilar tissue regions become mixed, reducing the ability to distinguish distinct patterns. To address this, we introduce Boosted Adaptive Radius Graph (BARG), a novel graph modelling strategy tailored for Haematoxylin and Eosin (H&E)-stained Tissue MicroArray (TMA) images. BARG improves upon the traditional Fixed Radius Graph (FRG) approach by incorporating an adaptive, tissue-specific edge threshold and a two-hop edge promotion mechanism to enhance message passing and maintain connectivity without compromising homophily. The adaptive threshold, termed Adaptive Radial Proximity (ARP), is determined for each graph using statistical analysis of Local Density Features (LDFs) derived from FRG-based graphs and is further refined using a globally optimised scaling factor across the dataset. We evaluate BARG using a dataset of 1000 TMA images with balanced positive and negative samples for training and a test set of 554 images (287 positive and 257 negative), with each patient contributing one image. Graph node features are extracted via a pre-trained VGG16 Convolutional Neural Network (CNN) by processing small image patches centred at nucleus detection peaks. Compared to the FRG-based models, BARG yields notable performance gains, achieving 78% accuracy, 75% sensitivity, and 81% specificity, marking a 4% improvement in accuracy and an 8% increase in sensitivity. BARG also reaches an AUC-ROC of 0.85, a 3% enhancement over FRG, while preserving structural and contextual tissue relevance. These results position BARG as a robust, scalable solution for graph modelling in histopathology image analysis, suitable for broader applications in computational pathology.

Keywords**:** Breast Cancer Hormonal Status, Estrogen Receptor Status, Deep Learning, Graph Convolutional Networks, Digital Pathology, Machine Learning, Features Over-smoothing, Breast Cancer Biomarkers

1. Introduction

Breast cancer (BC) remains the most common cancer among women worldwide, with over 2.3 million new cases in 2020 [1]. A critical factor in the prognosis and treatment of invasive BC is the assessment of ERS, a predictive biomarker guiding hormone therapy decisions [2]. Clinical guidelines, including those from the American Society of Clinical Oncology, recommend testing for both Estrogen Receptors (ER) and Progesterone Receptors (PR) in all invasive BC patients. Immunohistochemistry (IHC) is the standard method for evaluating ERS and PR status (PRS), with positivity defined as at least 1% of carcinoma cells showing staining of any intensity [3]. About 70% of BC patients are ER-positive, making ERS the most influential marker for hormone therapy eligibility [4]. Although ER and PR are often co-expressed, discordant cases are rare, and ERS is generally the primary determinant for hormone therapy. Despite widespread use, IHC-based ERS assessment has notable limitations. It requires costly reagents, trained personnel, and is time-consuming. More critically, IHC interpretation is subjective, relying on the visual estimation of stained nuclei, which introduces variability and human error [5]. Technical factors such as tissue handling, fixation, antibody selection, and thresholds also contribute to inconsistencies [2]. Studies report up to 20% inaccuracy in IHC-based ERS results, causing false positives or negatives [3]. These challenges highlight the need for more objective, reproducible, and scalable ERS assessment methods. H&E staining remains the primary histopathological tool for BC diagnosis. Pathologists evaluate H&E slides for morphology, spatial arrangement, and cell density [6].

Recent AI advances have shown that features from H&E images can correlate with ERS—even when not visually apparent [5, 7, 8, 9, 10]. Most AI methods use CNNs [5, 7, 8, 9] or nuclei morphometric features as CNN inputs [10].

Proceedings of the 11th World Congress on New Technologies (NewTech'25)
Paris, France - August, 2025
Paper No. ICBB 160
DOI: 10.11159/icbb25.160

However, CNNs are limited by local receptive fields, making them less effective at capturing long-range spatial relationships crucial to tissue structure. Additionally, CNNs require large annotated datasets and often yield biologically uninterpretable features. Graph-based representation learning has emerged as a powerful alternative in computational pathology. In cell-graphs, nuclei serve as nodes, with edges encoding spatial relationships—enabling modelling of complex inter-cellular dependencies [6, 11, 12, 13, 14]. GCNs have successfully classified H&E slides into diagnostic categories like normal, benign, in-situ, and invasive carcinoma [15]. GCNs excel in capturing spatial relationships but are highly dependent on effective graph structures and informative node features. Classifying H&E images using graph-based modelling involves representing cells as graph nodes, with edges defined via spatial proximity—typically using Euclidean distance thresholds. Properly designed graphs capture tissue-specific cell organisation. Existing studies mainly use FRG strategy for cell-graph modelling with a radial proximity threshold, applying a global threshold to define edges.

Despite advancements in computational pathology, graph-based classification of BC ERS from H&E-stained images remains largely unexplored. We address this gap by introducing a novel feature-embedded graph modelling strategy tailored specifically for BC ERS classification. Our approach incorporates cell organization into graph construction and integrates deep features extracted from a pre-trained VGG16, a powerful CNN model. This method aims to improve classification accuracy, sensitivity, and AUC-ROC compared to the conventional FRG strategy. We extend FRG into an enhanced framework, termed BARG, by introducing several key innovations. First, we construct FRG-based graphs using an optimised connectivity threshold applied across the full dataset. From these graphs, we extract a tissue-specific parameter derived from the Cumulative Distribution Function (CDF) of nodes' Local Density Features (LDFs), which guides the graph modelling process. To improve node communication in GCNs, we apply a 2-hop edge promotion strategy to link each node directly to its second-hop neighbours, enhancing the graph connectivity. The tissue-specific parameter is further refined using a globally optimised scaling constant. This multi-stage pipeline enables more precise modelling of tissue microenvironments, resulting in improved classification outcomes.

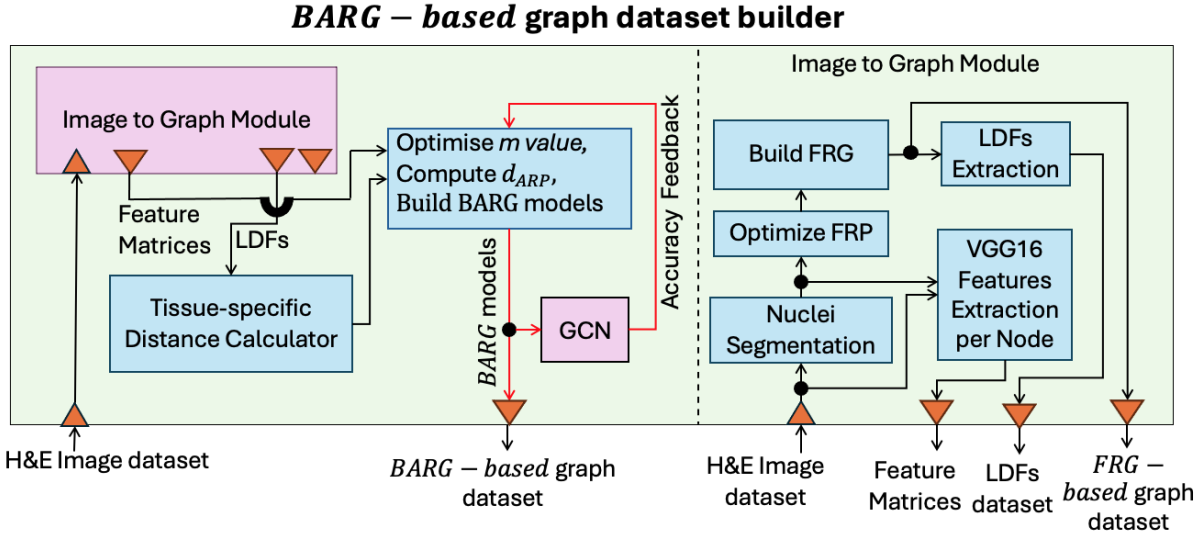

Fig. 1: BARG strategy for graph modelling of H&E-stained histology images

2. Materials and Methods

We hypothesise that ERS in invasive breast cancer can be accurately predicted from H&E-stained slides by modelling both cellular morphology and inter-cellular spatial relationships, enhanced by deep learning features.

Figure 1 provides an overview of our proposed graph construction methodology, BARG strategy, which consists of the following steps:

Proceedings of the 11th World Congress on New Technologies (NewTech'25)
Paris, France - August, 2025
Paper No. ICBB 160
DOI: 10.11159/icbb25.160

2.1. Data Acquisition

We use the publicly available Genetic Pathology Evaluation Centre (GPEC) databank [17-19], comprising 17 H&E-stained TMA slides from patients with invasive breast cancer, each annotated with pathologist-assessed ERS. After quality control, we curated a cohort of 1554 patients, each with a single TMA image containing at least 600 segmented nuclei. The dataset was split into a balanced training set (1000 images: 500 ER-positive, 500 ER- negative) and an independent test set (554 images: 287 ER-positive, 257 ER-negative). Each TMA image measures 650 × 800 pixels, corresponding to a 0.6 mm diameter tissue core.

2.2. Nuclei segmentation

Nuclei segmentation is performed using a multi-step image processing pipeline: (1) image upscaling, (2) background removal, (3) conversion to HSV and extraction of the brightness channel, (4) Otsu thresholding, (5) filling holes in detected nuclei, and (6) watershed segmentation to separate overlapping nuclei [20]. This approach, adapted from [10], ensures accurate identification of nuclei for subsequent graph construction.

2.3. FRG Strategy

We consider the nuclei detected in Section 2.2 as graph nodes to build the graph model defined as $G = \{V, E, A\}$ for a given H&E-stained TMA image. Here, V is a finite set of graph nodes exhibiting at least one edge in the graph model, E is the set of graph edges, and A is an unweighted connectivity matrix constructed based on spatial proximity between pairs of nuclei (nodes). For the FRG strategy, we establish edges using a constant threshold d_{max} across all images, $A_{FRG,q}$ is the graph adjacency matrix built with FRG strategy for the qth image in dataset:

$$A_{FRG,\,q}(i,j) = \begin{cases} 1, & if \sqrt{(x_i - x_j)^2 + (y_i - y_j)^2} \le d_{max} \\ 0, & otherwise \end{cases}, \quad i, j = 0,1, \ldots, N-1 \qquad (1)$$

where d_{max} is a critical hyper-parameter that determines the spatial connectivity threshold in FRG construction. We optimise this parameter through grid search to maximise the ERS classification accuracy on our BC TMA image dataset, ensuring optimal graph connectivity for effective message passing in GCNs.

2.4. BARG Strategy

For the qth FRG model in our dataset, denoted as $G_{FRG,q}$, we compute LDF (i, q) for its ith node as a normalized score representing its spatial proximity to its three closest neighbours, if they exist, as follows:

$$LDF(i,q) = \begin{cases} 1 - \frac{1}{d_{max}} \cdot \frac{\sum_{j=1}^{\min(\deg(i,q))} r_{ij}}{\min(3, \deg(i,q))} & if \ \deg(i,q) \ge 1, \\ 0, & otherwise \end{cases} \qquad (2)$$
$$i = 0, 1, \ldots, N-1$$

where r_{ij} is the distance between node i and its jth closest neighbour in the graph. deg(i, q) is degree of node i in $G_{FRG,q}$ measured as $\deg(i,q) = \sum_{j=0,\ j \ne i}^{N-1} A_{FRG,\,q}(i,j)$. To determine the tissue-specific distance for $G_{FRG,q}$ as $D_{TS}(G_q)$, we analyse the CDF of LDFs in this graph model by plotting CDF curve for LDFs across all nodes. The 80th percentile in the CDF curve of qth graph, denoted as $T_{80}(G_q)$, is selected as our fixed reference point. This percentile is converted to a distance value as shown in Eq (3).

$$D_{TS}(G_q) = \left(1 - T_{80}(G_q)\right) d_{max} \qquad (3)$$

Proceedings of the 11th World Congress on New Technologies (NewTech'25)
Paris, France - August, 2025
Paper No. ICBB 160
DOI: 10.11159/icbb25.160

After measuring the tissue-specific parameter for each FRG model in our dataset as $\{D_{TS}(q) \mid q \in [0, N-1]\}$, we adjust these tissue specific parameters using a multiplier m to define ARP threshold for the qth graph noted as $d_{ARP}(q)$ as

$$d_{ARP}(G_q) = m\, D_{TS}(G_q) \tag{4}$$

This parameter m is later optimised via grid search using the entire BARG-based graph dataset (constructed using Eq (6)) in conjunction with our GCN classifier (refer to Section 2.6.) to maximize classification accuracy.

The adjacency matrix for qth Adaptive Radial Proximity Graph model, denoted as ARG(q), is defined as

$$A_{ARG,\,q}(i,j) = \begin{cases} 1, & if \sqrt{(x_i - x_j)^2 + (y_i - y_j)^2} \le d_{ARP}(G_q) \\ 0, & otherwise \end{cases}, \quad i, j = 0,1, \ldots, N-1 \tag{5}$$

We enhance connectivity in ARG(q) model through a targeted rewiring strategy that converts the 2-hop neighbours of each node into direct 1-hop neighbours defining the final adjacency matrix from BARG strategy for qth graph as

$$A_{BARG,q} = A_{ARG,q} \times A_{ARG,q} \tag{6}$$

Converting 2-hop edges into 1-hop edges increases intra-cluster edge density and enhances message passing efficiency. After building the Adjacency matrices using Eq (6) for different values of m in Eq (4), parameter m is optimised through grid search to achieve the maximum accuracy from GCN (refer to Section 2.6.) using the BARG-based graph dataset. Figure 1 shows a figurative abstract for BARG and FRG graph construction strategies.

2.5. Graph Feature Matrix

The graph feature matrix $X \in \mathbb{R}^{N \times d}$ where N is the number of nodes and d is the number of features is constructed using a VGG16 model pre-trained on ImageNet [21], a powerful CNN employed as a feature extractor with its top classification layer removed. For each nucleus - modelled as a graph node - a feature vector is extracted from an image patch of size p × p, centred at the nucleus detection peak.

2.6. GCN Classifier

Following [16], we build a GCN by implementing the layer-wise propagation rule for spectral graph convolution operations. For the lth layer, the propagation rule is defined as

$$H^{(l+1)} = \sigma(\tilde{D}^{-\frac{1}{2}} A \tilde{D}^{-\frac{1}{2}} H^{(l)} W^{(l)}) \tag{7}$$

where A is the adjacency matrix, D is the Degree matrix, $H^{(l)}$ represents the input feature matrix to the lth graph convolution layer, and $W^{(l)}$ is the trainable weight matrix for the lth graph convolution layer, σ denotes the activation function. $H^{(0)}$ is the graph feature matrix X. This GCN model consists of two graph convolutional layers, with the number of filters in each layer denoted by the hyperparameters f_1 and f_2, which are optimised during experimentation.

3. Results and Discussion

The FRG dataset is constructed using a threshold value of d_{max}=40, which is optimised for the dataset via grid search according to Eq (1). LDFs are then computed for all nodes in each graph model built using the FRG method as defined in Eq (2). Additionally, the tissue-specific distance for the qth graph, $D_{TS}(G_q)$, was calculated using Eq (3). Then, a multiplier $m = 3$ was determined via grid search by computing $d_{ARP}(G_q)$ values using Eq (4), constructing BARG-based dataset through Eqs (5) and (6), and evaluating its performance using our GCN classifier. The value of m that yielded the highest classification accuracy using the BARG-based dataset was selected. After finding the global

Proceedings of the 11th World Congress on New Technologies (NewTech'25)
Paris, France - August, 2025
Paper No. ICBB 160
DOI: 10.11159/icbb25.160

parameter *m* and the tuned tissue-specific parameters $\{D_{TS}(q) \mid q \in [0, N-1]\}$, we computed $\{d_{ARP}(q) \mid q \in [0, N-1]\}$ values using Eq (4) to build adjacency matrices for ARG-based models using Eq (5). Then, we build adjacency matrices for BARG-based models using Eq (6). We train and validate a GCN classifier as explained in Eq (7) on FRG–based dataset denoted as GCN(FRG). We also train and validate another GCN on the BARG–based dataset denoted as GCN(BARG). In our experiments with the GCN classifier, the number of filters in two graph convolutional layers denoted as f_1 *and* f_2 were optimised and set to $f_1 = f_2 = 512$. The model was trained using the binary cross-entropy loss function and the optimiser used was Adam with a learning rate of 0.0001. The graph feature matrix X was constructed using feature vectors extracted as described in Section 2.5. Specifically, by setting p=33, image patches of size 33×33 were extracted, centred at the detection peak of each nucleus, resulting in feature vectors of dimension $d = 512$. We used $A_{FRG,q}$ from Eq (1), and $A_{BARG,q}$ from Eq (6) as adjacency matrix A in Eq (7) to train GCN(FRG) and GCN(BARG) models, respectively. Table 1 presents a comparison of accuracy metrics between these two models. Representing accuracy as acc., AUC-ROC as AUC, sensitivity as Sens., specificity as Spec., Positive Predictive Value as PPV, Negative Predictive Value as NPV, Area Under Precision Recall curve as AUPR, and F1-score as F1. In comparison to FRG-based models, BARG delivers significant performance improvements, attaining 78% accuracy, 75% sensitivity, and 81% specificity—representing a 4% increase in accuracy and an 8% boost in sensitivity. It also achieves an AUC-ROC of 0.85, reflecting a 2% gain over FRG, while effectively maintaining structural integrity and tissue context. Figure 2 presents the ROC curves of GCN(FRG) and GCN(BARG) on the left, and their corresponding Precision–Recall curves on the right.

Table 1: Performance Metrics GCN(BARG) and GCN(FRG)

Classifier	acc.	AUC	Sens.	Spec.	PPV	NPV	AUPR	F1
GCN(BARG)	0.778	0.847	0.746	0.813	0.817	0.741	0.851	0.780
GCN(FRG)	0.741	0.816	0.672	0.817	0.804	0.691	0.833	0.732

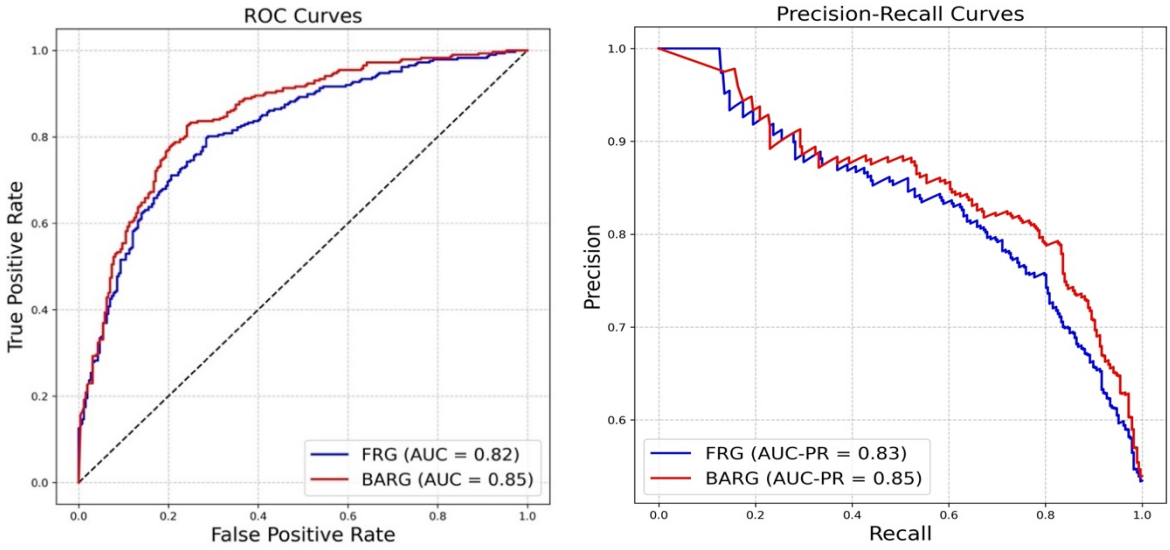

Fig. 2: Performance comparison of FRG and BARG strategies. left: ROC-Curves Comparison, right: PR-Curves Comparison.

These findings establish BARG as a reliable and scalable approach for graph modelling in histopathology image analysis, with strong potential for broader use in computational pathology. Feature over-smoothing is a known issue in heterogeneous graph structures, where dissimilar node features become indistinguishable during message passing. To address this, our method enhances graph homophily through the use of ARP threshold for graph construction while maintaining strong connectivity by promoting 2-hop edges to 1-hop, ensuring effective message propagation in GCN.

4. CONCLUSIONS

We propose BARG, the first adaptive graph modelling strategy that accounts for variable tissue structures by measuring local cell density percentiles, enabling tissue-specific graph construction. We use LDFs to define a tissue-specific threshold for connectivity, while also applying a dataset-wide adjustment to optimise this threshold for improved GCN performance. Using BARG for graph construction significantly enhances BC ERS classification accuracy with a GCN classifier, compared to the traditional FRG strategy. BARG provides a robust and generalisable framework for graph modelling and can be readily extended to other graph-based histology image classification tasks.

REFERENCES

[1] Sung, H., Ferlay, J., Siegel, R. L., Laversanne, M., Soerjomataram, I., Jemal, A., and Bray, F., 2021. Global cancer statistics 2020: GLOBOCAN estimates of incidence and mortality worldwide for 36 cancers in 185 countries. CA: A Cancer Journal for Clinicians, 71(3), 209–249.

[2] Gown, A. M., 2008. Current issues in ER and HER2 testing by IHC in breast cancer. Modern Pathology, 21(2), S8–S15.

[3] Hammond, M.E.H., Hayes, D.F., Dowsett, M., Allred, D.C., Hagerty, K.L., Badve, S., Fitzgibbons, P.L., Francis, G., Goldstein, N.S., Hayes, M. and Hicks, D.G., 2010. American Society of Clinical Oncology/College of American Pathologists guideline recommendations for immunohistochemical testing of estrogen and progesterone receptors in breast cancer. *Journal of clinical oncology*, *28*(16), pp.2784-2795.

[4] Lumachi, F., Brunello, A., Maruzzo, M., Basso, U., and Basso, S. M. M., 2013. Treat-ment of estr-ogen receptor-positive breast cancer. Current Medicinal Chemistry, 20(5), 596–604.

[5] Shamai, G., Binenbaum, Y., Slossberg, R., Duek, I., Gil, Z., and Kimmel, R., 2019. Artificial intelligence algorithms to assess hormonal status from tissue microarrays in patients with breast cancer. JAMA Network Open, 2(7), e197700.

[6] Ahmedt-Aristizabal, D., Armin, M. A., Denman, S., Fookes, C., and Petersson, L., 2022. A survey on graph-based deep learning for computational histopathology. Computerized Medical Imaging and Graphics, 95, 102027.

[7] Couture, H.D., Williams, L.A., Geradts, J., Nyante, S.J., Butler, E.N., Marron, J.S., Perou, C.M., Troester, M.A. and Niethammer, M., 2018. Image analysis with deep learning to predict breast cancer grade, ER status, histologic subtype, and intrinsic subtype. *NPJ breast cancer*, *4*(1), p.30.

[8] Naik, N., Madani, A., Esteva, A., Keskar, N. S., Press, M. F., Ruderman, D., Agus, D. B., and Socher, R., 2020. Deep learning-enabled breast cancer hormonal receptor status determination from base-level H&E stains. Nature Communications, 11(1), 5727.

[9] Gamble, P., Jaroensri, R., Wang, H., Tan, F., Moran, M., Brown, T., Flament-Auvigne, I., Rakha, E.A., Toss, M., Dabbs, D.J. and Regitnig, P., 2021. Determining breast cancer biomarker status and associated morphological features using deep learning. *Communications medicine*, *1*(1), p.14.

[10] Rawat, R. R., Ruderman, D., Macklin, P., Rimm, D. L., and Agus, D. B., 2018. Correlating nuclear morphometric patterns with estrogen receptor status in breast cancer pathologic specimens. NPJ Breast Cancer, 4(1), 32.

[11] Sharma, H., Zerbe, N., Lohmann, S., Kayser, K., Hellwich, O., and Hufnagl, P., 2015. A review of graph-based methods for image analysis in digital histopathology. Diagnostic Pathology, 1(1).

[12] Anand, D., Gadiya, S., and Sethi, A., 2020, March. Histographs: Graphs in histopathology. In Medical Imaging 2020: Digital Pathology (Vol. 11320, pp. 150–155). SPIE.

[13] Wang, J., Chen, R. J., Lu, M. Y., Baras, A., and Mahmood, F., 2020, April. Weakly supervised prostate TMA classification via graph convolutional networks. In 2020 IEEE 17th International Symposium on Biomedical Imaging (ISBI) (pp. 239–243). IEEE.

[14] Zhou, Y., Graham, S., Alemi Koohbanani, N., Shaban, M., Heng, P. A., and Rajpoot, N., 2019. CGC-Net: Cell graph convolutional network for grading of colorectal cancer histology images. In Proceedings of the IEEE/CVF International Conference on Computer Vision Workshops (pp. 0–0).

[15] Gao, Z., Lu, Z., Wang, J., Ying, S., and Shi, J., 2022. A convolutional neural network and graph convolutional network based framework for classification of breast histopathological images. IEEE Journal of Biomedical and Health Informatics, 26(7), 3163–3173.

[16] Kipf, T. N., and Welling, M., 2017. Semi-supervised classification with graph convolutional ne-tworks. In International Conference on Learning Representations (ICLR).

[17] Cheang, M.C., Treaba, D.O., Speers, C.H., Olivotto, I.A., Bajdik, C.D., Chia, S.K., Goldstein, L.C., Gelmon, K.A., Huntsman, D., Gilks, C.B. and Nielsen, T.O., 2006. Immunohistochemical detection using the new rabbit monoclonal antibody SP1 of estrogen receptor in breast cancer is superior to mouse monoclonal antibody 1D5 in predicting survival. *Journal of clinical oncology*, *24*(36), pp.5637-5644.

[18] Welcome to GPEC Bliss Server Images, viewed 3 May 2023, www.gpecdata.med-.ubc.ca/images/bliss/.

[19] Genetic Pathology Evaluation Centre, viewed 2 Jul 2022, http://www.gpecimage.ubc.ca/.

[20] Schindelin, J., Arganda-Carreras, I., Frise, E., Kaynig, V., Longair, M., Pietzsch, T., Preibisch, S., Rueden, C., Saalfeld, S., Schmid, B. and Tinevez, J.Y., 2012. Fiji: an open-source platform for biological-image analysis. *Nature methods*, *9*(7), pp.676-682.

[21] Deng, J., Dong, W., Socher, R., Li, L. J., Li, K., and Fei-Fei, L., 2009, June. ImageNet: A large-scale hierarchical image database. In 2009 IEEE Conference on Computer Vision and Pattern Recognition (pp. 248–255). IEEE.